Translational Oncology
www.transonc.com

Volume 8 Number 1 February 2015 pp. 25–34 25

Quantitative Ultrasound Spectroscopic Imaging for Characterization of Disease Extent in Prostate Cancer Patients[1]

Ali Sadeghi-Naini[*,†,‡,§], Ervis Sofroni[*,†,¶], Naum Papanicolau[*,†,¶], Omar Falou[*,†,‡,§], Linda Sugar[#], Gerard Morton[†,§], Martin J. Yaffe[*,‡], Robert Nam[,††], Alireza Sadeghian[¶], Michael C. Kolios[‡,‡‡], Hans T. Chung[†,§] and Gregory J. Czarnota[*,†,‡,§]**

*Physical Sciences, Sunnybrook Research Institute, Sunnybrook Health Sciences Centre, Toronto, ON, Canada M4N 3M5; [†]Department of Radiation Oncology, Odette Cancer Centre, Sunnybrook Health Sciences Centre, Toronto, ON, Canada M4N 3M5; [‡]Department of Medical Biophysics, Faculty of Medicine, University of Toronto, Toronto, ON, Canada M4N 3M5; [§]Department of Radiation Oncology, Faculty of Medicine, University of Toronto, Toronto, ON, Canada M4N 3M5; [¶]Department of Computer Science, Ryerson University, Toronto, Ontario, Canada M5B 2K3; [#]Department of Pathology, Sunnybrook Health Sciences Centre, Toronto, Ontario, Canada M4N 3M5; **Division of Urology, Sunnybrook Health Sciences Centre, Toronto, Ontario, Canada M4N 3M5; [††]Department of Surgery, Faculty of Medicine, University of Toronto, Toronto, Ontario, Canada M4N 3M5; [‡‡]Department of Physics, Ryerson University, Toronto, Ontario, Canada M5B 2K3

Abstract

Three-dimensional quantitative ultrasound spectroscopic imaging of prostate was investigated clinically for the noninvasive detection and extent characterization of disease in cancer patients and compared to whole-mount, whole-gland histopathology of radical prostatectomy specimens. Fifteen patients with prostate cancer underwent a volumetric transrectal ultrasound scan before radical prostatectomy. Conventional-frequency (~5 MHz) ultrasound images and radiofrequency data were collected from patients. Normalized power spectra were used as the basis of quantitative ultrasound spectroscopy. Specifically, color-coded parametric maps of 0-MHz intercept, midband fit, and spectral slope were computed and used to characterize prostate tissue in ultrasound images. Areas of cancer were identified in whole-mount histopathology specimens, and disease extent was correlated to that estimated from quantitative ultrasound parametric images. Midband fit and 0-MHz intercept parameters were found to be best associated with the presence of disease as located on histopathology whole-mount sections. Obtained results indicated a correlation between disease extent estimated noninvasively based on midband fit parametric images and that identified histopathologically on prostatectomy specimens, with an r^2 value of 0.71 ($P < .0001$). The 0-MHz intercept parameter demonstrated a lower level of correlation with histopathology. Spectral slope parametric maps offered no discrimination of disease. Multiple regression analysis produced a hybrid disease characterization model ($r^2 = 0.764$, $P < .05$), implying that the midband fit biomarker

Address all correspondence to: Gregory J. Czarnota, Ph.D., M.D., FRCPC, Department of Radiation Oncology, and Physical Sciences, Odette Cancer Centre, and Sunnybrook Research Institute, Sunnybrook Health Sciences Centre, 2075 Bayview Ave, Suite T2-185, Toronto, Ontario, Canada M4N 3M5.
E-mail: Gregory.Czarnota@sunnybrook.ca

[1] Funding for this project was provided by the Terry Fox Foundation, the Natural Sciences and Engineering Research Council of Canada, and the Canadian Institutes of Health Research.

Received 15 September 2014; Revised 13 November 2014; Accepted 17 November 2014

1936-5233/15
http://dx.doi.org/10.1016/j.tranon.2014.11.005

had the greatest correlation with the histopathologic extent of disease. This work demonstrates that quantitative ultrasound spectroscopic imaging can be used for detecting prostate cancer and characterizing disease extent noninvasively, with corresponding gross three-dimensional histopathologic correlation.

Translational Oncology (2015) 8, 25–34

Introduction

Prostate cancer (PCa) is the most common malignancy diagnosed in men, with a high number of newly diagnosed cases totalling almost one third of all cancers detected in men annually [1–3]. PCa, most frequently diagnosed as adenocarcinoma of the prostate, is generally considered to respond successfully to available treatments if detected at an early gland-confined stage. Currently, acceptable treatments for PCa include watchful waiting, radiation therapy, and radical prostatectomy. Treatment selection is based upon the patient's stage of disease, age, and overall health. PCa screening is a very controversial topic; studies have shown mixed results and a lack of direct benefits with respect to PCa mortality rates of screened patients [4]. Similar results appear to be emerging for treated patients with low-grade, low-risk disease.

Traditional methods of PCa detection include testing of prostate-specific antigen (PSA) serum levels and digital rectal examination, with the former being the most widely used. PSA-based testing has been demonstrated to increase disease detection at an early stage [5]. This method is relatively cost effective, is reproducible, and has added a more objective criterion for disease identification. However, recent studies from the Prostate, Lung, Colorectal, and Ovarian Cancer Screening Trial and the European Randomized Study of Screening for Prostate Cancer regarding whether PSA screening improves cancer-specific survival have been conflicting [6,7]. This has prompted the United States Preventive Services Task Force to issue a recommendation statement against PSA screening in asymptomatic men, regardless of race, age, or family history [8]. Criticisms of the PSA assay as a screening test include its low sensitivity, low specificity, and appreciable false-positive rates resulting in exposure to side effects from transrectal biopsies, in addition to leading to an overdiagnosis bias causing unnecessary treatments and exposure to treatment-related complications [8–10].

Imaging of the prostate gland for diagnostic screening is feasible using various modalities such as magnetic resonance imaging (MRI), computed tomography, and ultrasound [11]. Although they can all be used to successfully image the prostate, transrectal ultrasound (TRUS) remains the most commonly used method. Whereas MRI has very good specificity, it is relatively costly, not widely available, and poorly tolerated by some patients, and it does not provide real-time imaging. In contrast, ultrasound-based solutions are frequently more preferable because they are inexpensive, portable, and typically better tolerated than MRI and they permit real-time imaging. The source of contrast in conventional TRUS B-mode images is the acoustic impedance mismatches between tissue types which result in different intensities of ultrasound backscattered signal. The hypoechoic areas demonstrated within these images are typically used in the clinic to identify putative areas of PCa. In this context, standard B-mode TRUS has generated relatively poor results in studies of prostatic cancer detection, and thus, it is generally used as a diagnostic follow-up technique rather than an initial screening modality. TRUS is also the primary imaging modality used in image-guided prostate biopsies. However, B-mode images of the prostate can vary based on ultrasound instrumentation used and individual user settings, which makes objective interpretations and definitive clinically-relevant conclusions difficult. Prior evidence has demonstrated that quantitative ultrasound (QUS) imaging of the prostate can increase the detection capability of biopsies by helping to target areas with a high likelihood of disease presence [12,13]. Those studies describe early pivotal applications of spectrum-analysis-based QUS techniques applied to PCa and biopsies in an effort to overcome the inability of standard ultrasound to detect PCa reliably.

QUS spectroscopy applies power-spectrum analysis techniques to process ultrasound backscattered radiofrequency (RF) signals to determine the bioacoustic properties of the underlying tissue for characterizing its microstructure. In this method, operator and instrument-setting variables are eliminated by normalizing ultrasound signals against a reference in a frequency-dependent manner. This technique has been demonstrated to be capable of detecting tumor response to treatment in preclinical models [14,15] and clinical settings [16–20] and differentiating between various tissue types [12,13,21,22] including benign versus malignant breast tumors in animal xenograft models [23,24]. In this context, a theoretical framework of power-spectrum analysis in tissue characterization was established by Lizzi et al., in which power-spectrum features were related to acoustic properties of tissue [25]. In a number of studies performed by that group, the use of tissue properties such as effective acoustic scatterer size, effective acoustic scatterer concentration, and acoustic impedance mismatch has been compared with clinical data and theoretical models. In those studies, the normalized power spectrum of the ultrasound backscattered RF signals was shown to carry rich information regarding tissue microstructure. Such information has been used for distinguishing different tissue types in the retina, liver, and prostate [26–28]; for characterizing, with high sensitivity and specificity, the presence of tumor deposits in lymph nodes *ex vivo* [29]; and for determining intravascular plaque composition and detecting high-risk lesion types, with good correlation to histopathology [30].

In the study here, we investigated the efficacy of QUS spectroscopy for the detection and extent characterization of disease noninvasively in PCa patients. Specifically, three-dimensional QUS spectral parametric maps were used to determine the areas of the prostate putatively affected by cancer. The estimated extents of disease were compared and correlated to those identified from serially-sectioned whole-mount histopathology of prostatectomy specimens as a gold standard approach for identifying cancerous areas. Ultrasound images and RF data were collected from 15 PCa patients before radical prostatectomy using a TRUS probe operating at ~ 5 MHz. Ultrasound images and RF data were collected for each patient volumetrically, in a

set of transverse planes separated by 5 mm. QUS spectral parameters were calculated using a sliding window approach to produce parametric maps of the 0-MHz intercept, midband fit (MBF), and spectral slope. Different values of the MBF and 0-MHz intercept parameters were determined to be associated with the presence of bulk disease as located on histopathology whole-mount sections separated similarly by 5 mm. The MBF parameter was found to have the highest level of correlation. In contrast, parametric maps generated from the spectral slope offered no discrimination for the cancerous areas. This work demonstrated that QUS spectroscopic parametric imaging can be applied to detect PCa noninvasively and to characterize the extent of disease within the prostate, with demonstrated gross histopathologic correlation. Such an approach can potentially facilitate PCa diagnosis with an increased sensitivity and specificity.

Material and Methods

Experimental Design and Data Collection

This study was conducted with institutional research ethics approval from Sunnybrook Health Sciences Centre and was open to all PCa patients meeting study criteria. Eligible patients included those confirmed histopathologically with adenocarcinoma of the prostate gland via a core biopsy procedure, with T2/T3 disease on histopathologic examination, consented for radical prostatectomy, not on androgen deprivation therapy, and with no prior chemotherapy or radiotherapy to the pelvis. In keeping with these, 15 eligible patients confirmed with localized palpable PCa were recruited for this study after obtaining written informed consent.

All the ultrasound data in this study were collected following standardized protocols for data acquisition. The ultrasonographer was blinded to the biopsy and histopathology results. Patients were scanned within 2 weeks before their radical prostatectomy in a dorsal lithotomy position. Volumetric ultrasound images and RF data were acquired in a set of transverse planes spanning the whole prostate and separated by 5 mm. The position and orientation of the scan planes were controlled using an in-house rail-based probe mount fixture. Data were collected using a Sonix RP system (Ultrasonix Medical Corporation, Richmond, BC, Canada) using a BPC8-4/10 128 element curvilinear array ultrasound transducer at the tip of a biplane transrectal probe (Vermon S.A., Tours, France), with a center frequency of ~5 MHz (3.5 to 6.5 MHz, −6 dB bandwidth). Acquired data consisted of ultrasound B-mode images and RF data collected with a sampling frequency of 40 MHz. The line density applied was 512 with an 85% sector width permitting for 430 RF lines per frame.

Histopathology Analysis

Patients underwent radical prostatectomy surgery within 1 to 2 weeks after ultrasound data collection. The prostate gland was removed *en bloc*, and labeled and orientated properly. Patient prostatectomy specimens were consequently fixed, sectioned, and mounted on whole-mount [31] histopathology slides. Fixation was performed in 5% formalin for up to 24 hours. Embedded tissue was sectioned in a serial manner using steps with 5-mm separation from apex to base at a 90° orientation perpendicular to the urethra, nominally matching the orientation at which ultrasound scans were performed. Sections were then cut for staining and microscopy using a Leica SM2500 motorized sliding microtome (Leica Microsystems, Concord, ON, Canada) and mounted on 2" × 3" glass slides. Staining was performed on each slide with hematoxylin and eosin. Stained glass slides were subsequently digitized at 1-μm resolution using a TISSUEscope 4000XT confocal scanner (Huron Technologies, Waterloo, ON, Canada). The digital images were examined by a pathologist for detecting and localizing malignancies and abnormal glandular structures. Specifically, areas of disease were contoured by the pathologist on images and were subsequently quantified using ImageJ (NIH, Bethesda, MD). Quantification was performed by calculating the total area of contoured disease in each prostate section relative to the area of the entire prostate in that section. Gross disease content was also determined within the prostate tissue for each specimen and compared to gross areas of abnormality identified over the corresponding QUS spectral parametric images, as described in the following section.

Ultrasound Data Analysis

Ultrasound RF data analysis was performed using linear regression analysis of the normalized power spectrum [12–15]. Ultrasound data were analyzed for all acquired planes through the scan volume and over the whole field of view for each plane using a sliding window approach (described further below). The power spectrum was calculated using a fast Fourier transform of the raw RF data for each scan line through the sliding window which was truncated using a Hamming function, and subsequently averaged. To remove the effects of system transfer functions, transducer beam forming, and diffraction artifacts, data were normalized using reference power spectra obtained from a glass-bead-embedded agar-gel phantom model [32,33]. Equation (1) describes the process of calculating the normalized power spectrum:

$$NPS(f) = \log\left(\frac{\sum_{i=M}^{N} \left| FFT(Hamming(e_t(t, x_i)))\right|^2}{\sum_{i=M}^{N} \left| FFT\left(Hamming\left(e_p(t, x_i)\right)\right)\right|^2}\right) \quad (1)$$

In this equation, NPS (f) represents normalized power spectrum (in dB_r) as a function of frequency (f); $e_t(t, x_i)$ and $e_p(t, x_i)$ are RF signals backscattered by tissue and phantom, respectively, as functions of time (t) and lateral position (x_i) at different RF lines ($i = M, M + 1, \ldots, N$).

Specifically, the average power spectrum obtained for each sliding window was normalized separately to a reference curve obtained from the same region of the phantom, with an equivalent location and size [Equation (1)]. This was carried out to more accurately account for the effects of attenuation and beam diffraction across the scan plane. Linear regression analysis was performed on the normalized power spectrum of RF data within a −6-dB window (bandwidth of 3.5 to 6.5 MHz) centered at the transducer center frequency (f_c) to generate a best-fit line [Equation (2)]. Parameters subsequently determined included the MBF [Equation (3)], the spectral slope, and the corresponding 0-MHz intercept [19,25]:

$$NPS(f) = Slope \times f + Intercept \quad (2)$$

$$MBF = Slope \times f_c + Intercept \quad (3)$$

Parametric images of these QUS spectral features were generated by sliding the analysis window over the entire field of view on a pixel-by-pixel basis. A histogram-based thresholding technique was applied

Table 1. Characteristics of the Patients

Pt. #	Age	PSA (ng/ml)	Gleason Score (out of 10)	Primary Gleason Component	Secondary Gleason Component	# Lymph Nodes Examined	# Lymph Nodes Involved	Stage of Primary Disease
1	65	11	9	4	5	5 + 3	0	pT3b
2	74	34.9	8	3	5	4	0	pT2
3	74	7.1	9	4	5	6	1	pT3a
4	68	8	7	3	4	0	0	pT3a
5	68	6.4	9	4	5	4	1	pT3a
6	53	5	7	3	4	5	0	pT3a
7	72	3.3	7	3	4	0	0	pT3a
8	67	7.8	7	4	3	0	0	pT3a
9	69	8.8	7	4	3	0	0	pT2
10	68	6.3	7	3	4	7	0	pT3a
11	63	4.8	7	3	4	2	0	pT2
12	65	5.5	7	4	3	0	0	pT2
13	59	6.2	7	3	4	0	0	pT2
14	67	4.6	7	4	3	6	0	pT2
15	60	45.1	9	4	5	7	0	pT3a

to segment the areas of putative abnormalities in parametric images within the confines of the prostate identified from the corresponding B-mode images [34,35]. The segmentation threshold was set to approximately one third (33%) of the mean data value for each parameter based on previous observations of decreased ultrasound signal intensity for cancerous areas within the prostate. The relative area of disease segmented in each image was consequently calculated with respect to the area of prostate in that image.

Statistical Analysis

Linear regression analysis (PASW Statistics 18, SPSS Inc., Chicago, IL) was carried out to evaluate potential correlations between the extent of disease identified based on whole-mount histopathology of prostatectomy specimens and those estimated noninvasively using QUS spectral parametric images. A multiple regression analysis was also performed to identify a model of the best combination of parameters for predicting the extent of disease as determined based on histopathology. The input parameters of the model included patient's age, PSA level, Gleason score determined from core biopsy specimens, and the MBF and 0-MHz-intercept-based extent of disease. A P value of less than .05 was considered in this analysis to identify variables with statistically significant contributions to the model.

Results

Characteristics of the PCa patients who participated in this study, along with their disease specification, have been summarized in Table 1. The patients had an average age of 66 years (SD = 5.7; range, 53 to 74), with a mean PSA level of 11 ng/ml (SD = 12.1; range, 3.3 to 45). The clinical T-stage of the cancer initially diagnosed was either T1c (87%) or T2a (13%). For study enrolment, subsequent examination indicated that all patients had T2 or greater digitally palpable disease. However, the pathologic T-stage identified from core biopsy specimens showed more advanced disease with pT2N0 (40%), pT3aN0 (40%), pT3aN1 (13%), and pT3bN0 (7%). The histopathology analysis indicated Gleason scores of 3 + 4 (40%), 4 + 3 (27%), 3 + 5 (7%), and 4 + 5 (27%) for the patients. Based on the histopathology of radical prostatectomy specimens, the areas of prostate involved with cancer were 13% on average.

A representative ultrasound B-mode image of a study patient's prostate, along with the corresponding QUS parametric images of the MBF, 0-MHz intercept, and spectral slope, is presented in Figure 1. Whereas the MBF and 0-MHz parametric images depicted area of putative disease (dark regions within the prostate, further described below) relatively well, the contrast in the parametric map of the spectral slope was relatively poor. Figure 2 presents a visual representation of QUS spectroscopic imaging for prostate tissue characterization using data from a representative patient acquired at four transverse planes throughout the prostate separated by 5 mm. Figure 2*A* shows standard B-mode images obtained without any additional signal modifications. To extract quantitative information regarding underlying prostate tissue microstructure to enable objective disease extent evaluation, spectral parametric images of the MBF and 0-MHz intercept were generated for the same set of scan planes from the corresponding ultrasound RF data. The MBF parametric images obtained are presented in Figure 2*B*, indicating relative differences of 9 to 15 dB_r between the gross areas of putative disease and the areas of normal tissue within the prostate. Visual evaluations demonstrated that the QUS spectral parametric maps generated had enough sensitivity and specificity to permit generally the delineation of areas of bulk disease in the prostate by an

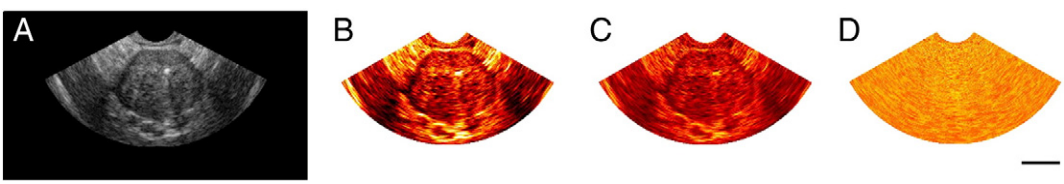

Figure 1. Representative ultrasound image and QUS spectral parametric maps acquired for a PCa patient. (A) Ultrasound B-mode image of prostate and (B-D) the corresponding QUS spectral parametric images of the MBF (B), 0-MHz intercept (C), and spectral slope (D). Scale bar represents ~1 cm.

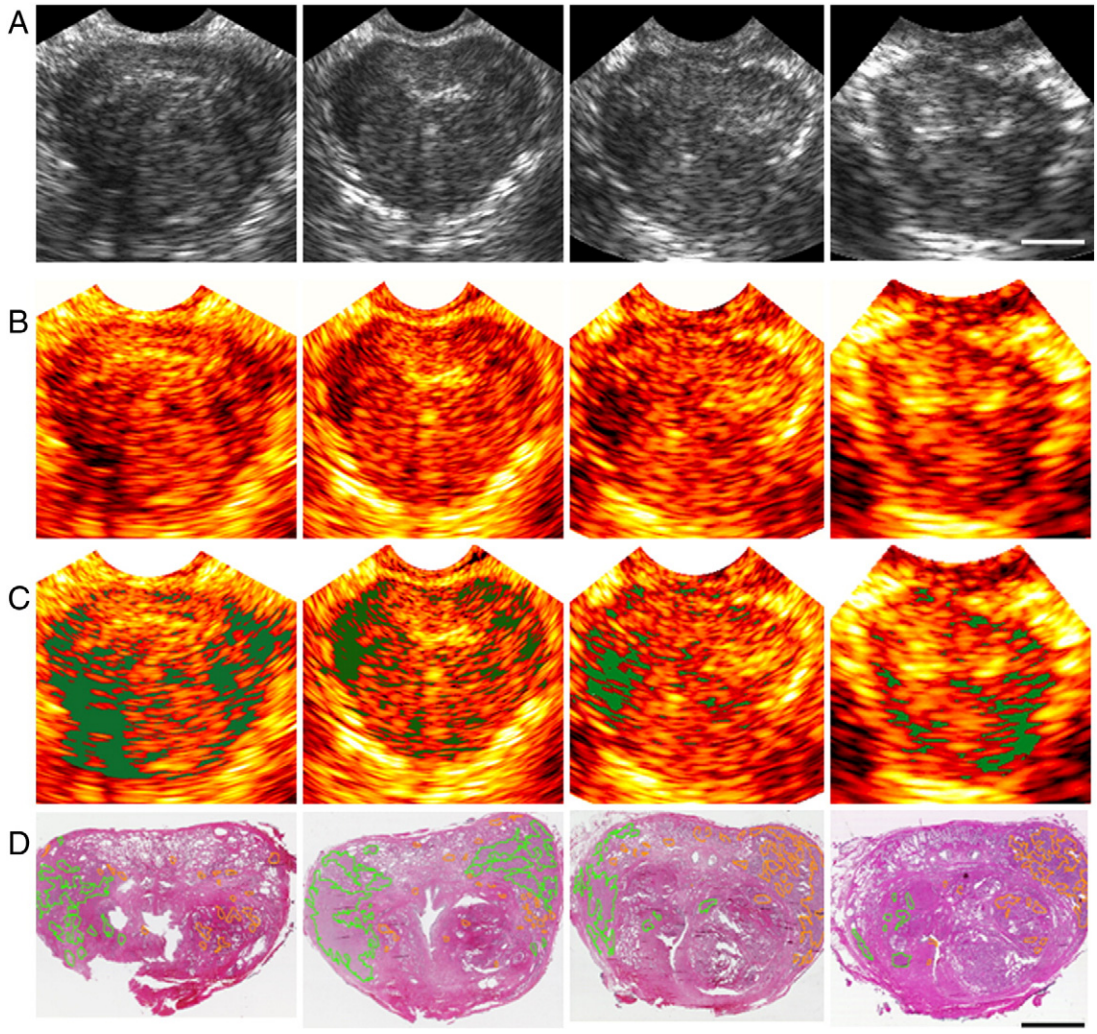

Figure 2. Ultrasound B-mode images, QUS spectral parametric maps, and the whole-mount histopathology slides corresponding to a representative PCa patient. Data were acquired at four transverse scan planes throughout the prostate. (A) Ultrasound B-mode images and (B) the corresponding MBF parametric images acquired at four transverse scan planes throughout the prostate. Scale bar represents ~1 cm. (C) The MBF parametric images with identified areas of putative disease segmented over the images. (D) The whole-mount histopathology slides obtained from sections of prostatectomy specimen which nominally correspond to the ultrasound scan planes. Areas outlined in green and orange indicate tumor and hyperplastic areas of abnormality, respectively. Scale bar represents ~1 cm.

oncologist. Using a histogram-based thresholding approach, suspicious areas of disease were segmented, as shown in Figure 2*C*. Figure 2*D* illustrates digital images of the whole-mount histopathology slides obtained from sections of the corresponding prostatectomy specimen, separated by 5 mm and roughly matched to the position and orientation of the ultrasound scan planes presented in Figure 2, *A-C*. Disease extent was estimated from the QUS spectral parametric images and histopathology slides in the form of relative areas of the prostate affected by cancer (presented in Figure 3). The plots presented in this figure suggest that the relative areas of disease in the histopathology images have a relatively good correspondence with suspicious areas of disease identified noninvasively using the MBF parametric images but demonstrate a lower level of correlation with those identified using the parametric images of the 0-MHz parameter. Specifically, relative areas of 12 ± 4%, 13 ± 5%, and 7 ± 2% were the average extent of disease estimated from whole-mount histopathology slides, and the parametric images of MBF and 0-MHz intercept, respectively.

Figure 4 demonstrates more comprehensive results of linear regression analyses performed using the data obtained from all patients to evaluate the levels of correlation between the extent of disease identified from the whole-mount histopathology slides and those predicted noninvasively using QUS spectroscopic imaging, at different transverse planes. Scatter plots of relative areas of disease detected based on histopathology versus the MBF and 0-MHZ intercept parametric imaging are presented in Figure 4, *A* and *B*, respectively, with the best line fitted to the data in addition to the corresponding 95% confidence interval. Linear regression analysis resulted in an r^2 value of 0.68 ($P < .0001$), with a 95% confidence interval ranging between 0.74 and 0.88 for the analysis using the MBF parametric images. However, the analysis did not result in a significant correlation for the 0-MHz intercept parametric image analysis, where an r^2 value of 0.06 ($P = .20$) was obtained, with a 95% confidence interval of −0.03 to 0.45.

Figure 5 presents the relative areas of disease estimated for each patient on average to further evaluate the efficacy of the technique in a scenario applicable more practically in clinic. Scatter plots of the

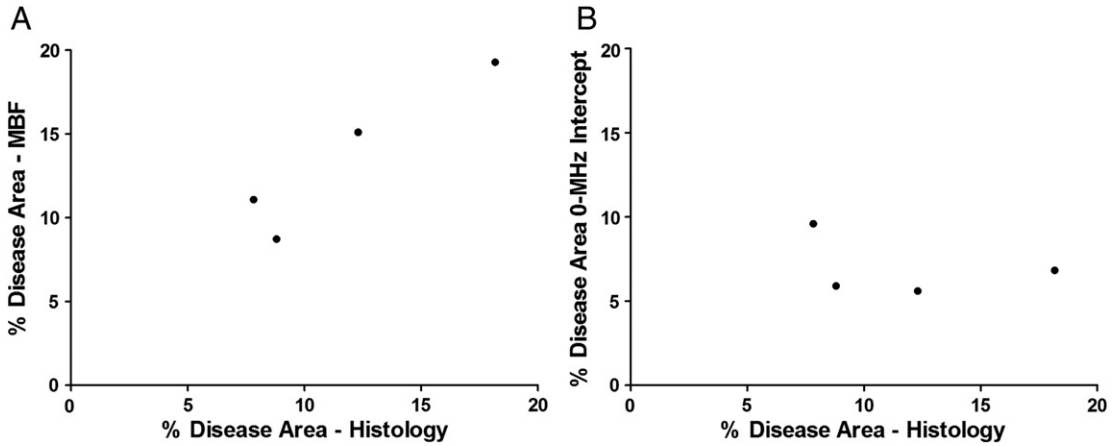

Figure 3. Extent of disease estimated at different scan planes for the representative patient of Figure 2. (A, B) Relative areas of disease identified from whole-mount histopathology versus those estimated noninvasively using the MBF (A) and 0-MHz intercept (B) parametric images.

average extent of the disease identified for the patients are presented based on histopathology and QUS spectroscopic imaging. Linear regression analyses were performed to find the lines fitted best to data and the corresponding 95% confidence intervals, as shown in this figure. The analyses resulted in correlations with r^2 values of 0.71 ($P < .0001$) and 0.10 ($P = .25$) and 95% confidence intervals of 0.58 to 0.95 and −0.23 to 0.71 for the MBF and 0-MHz intercept parametric imaging, respectively.

Relationships between the relative areas of disease estimated based on QUS spectroscopy and other clinical parameters, including the Gleason score, PSA level, and age of the patient, were investigated in the next step. A three-dimensional scatter plot of patient data is shown in Figure 6, demonstrating the Gleason score versus the corresponding PSA level and the MBF-based extent of disease for each patient. The figure implies that the two clinical parameters may not complement considerably the information provided by the MBF-based extent of disease. A multiple regression analysis was performed to better evaluate the contribution levels of the QUS-based estimations and the clinical parameters to a model predicting the histopathologic extent of disease. The multiple regression analysis resulted in a hybrid biomarker [Equation (4)] correlated to the relative area of disease identified histopathologically with an r^2 value of 0.76 ($P < .05$):

$$\begin{aligned} Hybrid\ biomarker = & (0.99 \times MBF\text{-}based\ extent\ of\ disease) \\ & + (0.16 \times Age) + (0.09 \times Gleasonscore) \\ & + (0.03 \times PSA\ level) \\ & + (-0.03 \times 0\text{-}MHz\ intercept\text{-}based\ extent \\ & \quad of\ disease) - \mathbf{13.09} \end{aligned} \tag{4}$$

Within the model's input parameters, the MBF-based extent of disease demonstrated the largest contribution to the prediction model ($P = .003$), followed by the age of the patient ($P = .28$). In addition, the MBF-based extent of disease was the only parameter that

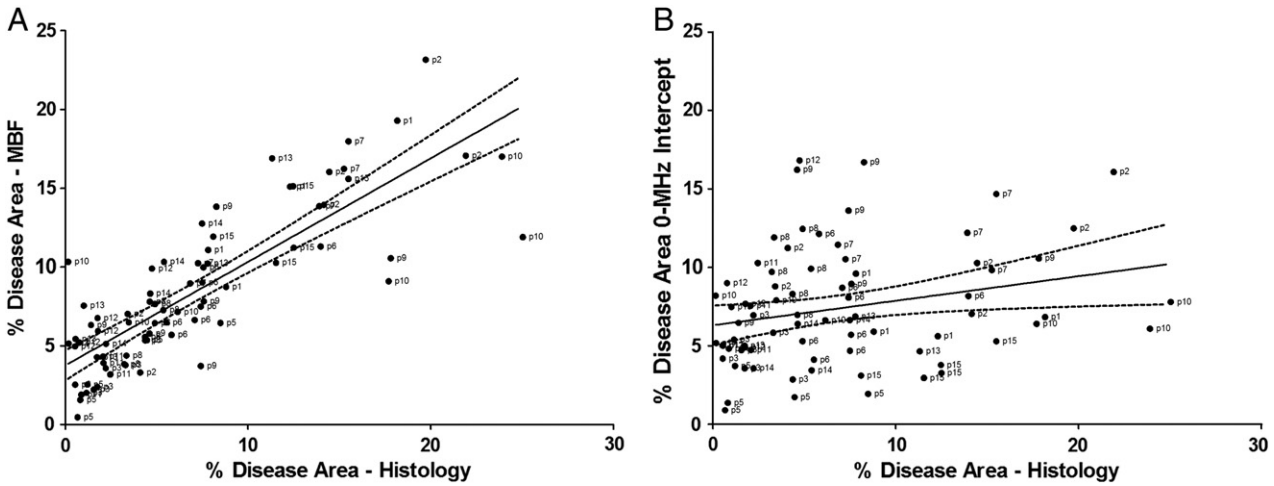

Figure 4. Scatter plots corresponding to the extent of disease estimated over different transverse planes of the prostate for all participating patients. (A, B) Relative areas of disease identified from whole-mount histopathology versus those estimated noninvasively using the MBF (A) and 0-MHz intercept (B) parametric images. The lines were fitted to data via linear regression analyses and presented within the 95% confidence intervals. The regression analysis resulted in r^2 values of 0.68 ($P < .0001$) and 0.06 ($P = .20$) for the MBF and 0-MHZ parametric imaging, respectively.

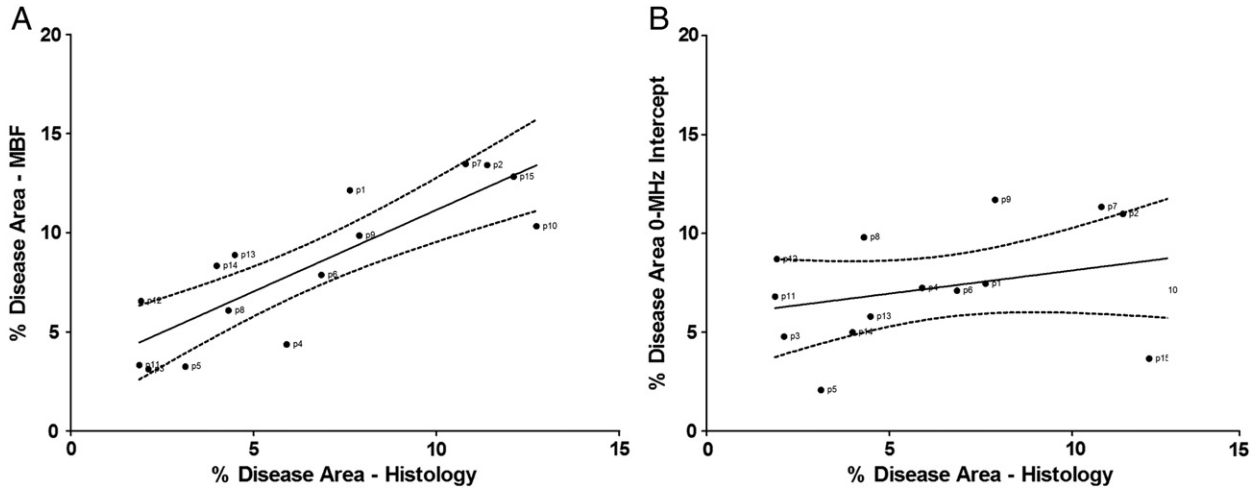

Figure 5. Extent of disease estimated on average for the patients. Plots shows relative areas of disease identified from whole-mount histopathology versus those estimated noninvasively using the (A) MBF and (B) 0-MHz intercept parametric images. The lines were fitted to data via linear regression analyses and presented within the 95% confidence intervals. The regression analysis resulted in r^2 values of 0.71 ($P < .0001$) and 0.10 ($P = .25$) for the MBF and 0-MHZ parametric imaging, respectively.

contributed significantly to the correlation of the resultant hybrid biomarker with the relative area of disease identified histopathologically. Results obtained for the multiple regression analysis have been summarized in Table 2.

Discussion and Conclusions

The efficacy of QUS spectroscopic imaging for predicating the histopathologic extent of PCa was investigated using the data acquired from 15 patients. Volumetric ultrasound images and RF data were acquired at clinically-relevant low frequencies in a set of transverse scan planes and processed using QUS spectroscopic techniques to estimate suspicious areas of disease within the prostate. Extent of disease estimated based on this type of three-dimensional QUS analysis of prostate tissue was compared and correlated to that identified in the corresponding serially-sectioned whole-mount histopathology of radical prostatectomy specimens.

Obtained results indicated the ability of QUS spectroscopic imaging to identify regions of the prostate with a high likelihood of disease presence. In regard to the three spectral parameters investigated, the MBF and the 0-MHz intercept showed a considerable degree of sensitivity to changes in the internal structure of the prostate gland. These parameters can be linked theoretically to effective acoustic scatterer size, effective acoustic scatterer concentration, and the acoustic impedance mismatch between the effective scatterers and the surrounding medium [25,36]. In contrast, spectral slope, which is predominantly linked only to the effective acoustic scatterer size [25,36], was not found to be sensitive to the presence of cancerous regions in prostate.

The results observed in this study were consistent with those of the previous landmark research by Feleppa et al. in their examination of prostate tissue using more limited core needle biopsy specimens [27,37,38]. Those studies demonstrated that the QUS methods could detect the presence of disease within prostate tissue as confirmed histopathologically using biopsy specimens. In the study here, volumetric ultrasound-based estimates of disease extent were compared and correlated to volumetric estimates of disease from whole-mount, whole-gland histopathology. In the research by Feleppa et al., considerable decreases were identified in the MBF and the 0-MHz intercept parameters estimated for cancer-affected prostate samples in comparison with disease-free prostate specimens [27,37,38]. There, neural network classifiers were also used to predict the likelihood of malignancy in the prostate compared to disease-free tissue, where a good performance was reported [39,40]. In addition, these QUS methods in general have been found applicable for detecting abnormalities in lymph nodes accurately and with high sensitivity and specificity using higher-frequency ultrasound [29]. Other investigations by Oelze et al. have also demonstrated that these methods can discriminate between benign and malignant tissues in

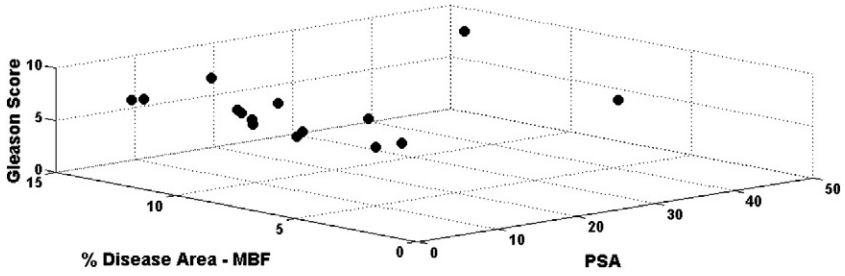

Figure 6. A three-dimensional scatter plot of the averaged data obtained for the patients, demonstrating the Gleason score versus the MBF-based relative area of disease and the PSA level for each patient.

Table 2. Results of the Multiple Regression Analysis for Modeling Histopathologic Extent of PCa

Input Variable	Coefficient	Standard Error	95% Confidence Interval		*P* Value
Age	0.16	0.14	−0.16	0.48	.28
PSA level	0.03	0.07	−0.12	0.18	.68
Gleason score	0.09	0.82	−1.76	1.94	.92
MBF-based extent of disease	0.99	0.25	0.44	1.56	.003 *
0-Mhz-intercept-based extent of disease	−0.03	0.30	−0.72	0.66	.917
Constant	−13.09	10.20	−36.2	9.98	.231

* Statistically highly significant ($P < .01$).

mouse breast tumor xenograft models [23,24]. In other applications of ultrasound-based tissue characterization, a number of studies have applied this type of spectral analysis for therapy response monitoring, demonstrating changes in QUS spectral parameters in association with the histological development of cell death [14–18,41–44]. Such methods have also been used to track the position of brachytherapy seeds in prostate [45–47] and to differentiate between vascular lesion types with good correlation to histopathology [48]. The study presented here features a volumetric QUS comparison with the three-dimensional whole-mount histopathology of prostatectomy specimens acquired from PCa patients. The results obtained suggest a good concordance between the relative areas (extent) of disease estimated for each patient based on the QUS parametric imaging and whole-mount histopathology. In addition, the MBF parameter was found to have the highest level of correlation with presence of cancerous areas within the prostate. This is consistent with observations of earlier work conducted by Feleppa et al. [26]. In the study here, variations were observed, as expected, in the range of values for each QUS parameter among patients. This was attributed to several factors that impact ultrasound imaging such as overall size, density, and internal microstructures of the prostate, which varied from patient to patient.

Extent of disease estimated using the MBF parametric imaging was comparable to that identified from histopathology, although the MBF-based relative areas of disease were observed to be relatively overestimated in general. Conversely, spectral 0-MHz intercept parametric images underestimated the relative areas of disease in most cases and did not demonstrate a comparable concordance with the results obtained from the histopathology. The high level of variability observed in the spectral slope parametric images of prostate tissue obtained for each patient suggests that the prostate gland is highly heterogeneous in terms of the size distribution of effective acoustic scatterers. This may partly be related to the influence on the higher order structure of glandular prostatic tissue by tightly packed carcinoma cells. In addition, factors such as the presence of widespread intraepithelial neoplasia in many of the prostate specimens, which also change microstructures of prostate tissue, may contribute to the variability of results. The findings of our study are in agreement with previous work with respect to the higher levels of variability exhibited by the spectral slope parameter and the inconsistency of that parameter in predicting potential areas of disease [27]. Histopathologically indicated areas of disease in our study were correlated relatively well to patient's age, which, as expected, likely reflects the extent of developed disease, but less correlated to PSA level. This may be a result of the fact that the majority of the patients who participated in this research had large clinically palpable T2/T3 disease.

A number of other ultrasound-based tissue characterization techniques have also been proposed for PCa detection and localization, such as those implemented in the HistoScanning system [49–51]. The application of such systems in routine clinical practice is still under evaluation particularly for smaller lesions [52,53]. The patients who participated in the study here had, by intent, relatively large palpable lesions, as the first phase of the study was primarily conducted for proof of principle. Further evaluation is necessary on the accuracy of the proposed framework for detecting and characterizing small and/or nonpalpable lesions. This has been planned to be investigated in the next phases of the study, where more patients with various lesion sizes will be recruited.

The extent of disease was estimated in this study using the relative area of disease, on average, within a number of separated transverse imaging planes spanning the whole prostate. Three-dimensional ultrasound data acquisition is, however, required through a continuous scan sweep or rotation to estimate the volume of disease within prostate. This has been planned to be investigated as a future work. Further investigation is also required to evaluate the efficacy of individual and hybrid QUS biomarkers to predict the tumor grade and stage of malignancy in PCa patients as important therapeutic characteristics of the disease.

In the study here, the radical prostatectomy specimens were sectioned in a serial manner at steps nominally matching the orientation at which ultrasound scans were performed. The ultrasound-based estimates of disease extent were compared and correlated to those obtained from histopathology within the whole volume of the prostate to further account for the possible slight mismatches between the imaging planes and histopathology cross sections. Whereas this approach is beneficial to obtain an approximate correlation between the noninvasive imaging biomarkers and the standard histopathologic findings, more accurate coregistration of QUS images and the histopathology slides is necessary in case a more precise correspondence is required for specific applications. Such a multimodal coregistration requires complicated processing blocks to be incorporated into the diagnostic framework and is currently being investigated in other studies [54–56].

Applications of other noninvasive imaging modalities for PCa diagnosis have been investigated in previous studies, including those based on single photon emission computed tomography, positron emission tomography, or MRI [11,57–59]. Unlike these imaging modalities that frequently need external contrast agents, the QUS techniques used here rely on inherent contrast between normal and cancerous tissues arising from differences in bioacoustical properties of these tissues and hence do not need the injection of any exogenous contrast agents. Ultrasound also has the advantages of low cost, rapid imaging speed, high resolution, and portability to complement the aforementioned imaging modalities.

In summary, the QUS-based diagnostic framework investigated in this study provides further impetus for using such noninvasive methods for the detection and characterization of disease. Specifically, the development of the histopathologically proven QUS parameters associated with the presence of disease in this study can form a basis for the identification and characterization of PCa and the evaluation of its response to treatment. In this context, the possibility of characterizing disease extent in PCa patients noninvasively can facilitate an early identification of high-/low-risk patients more accurately [60,61], an objective adjustment of treatment for patients on an individual basis [62], and the practice of personalized medicine in targeting PCa.

Acknowledgement

The first two authors have made equal contributions, as well as the last two authors. A.S.N. holds a Banting Postdoctoral Fellowship [63]. M.C.K. holds a Tier 2 Canada Research Chair [64] in Biomedical Applications of Ultrasound. G.J.C. holds a Cancer Care Ontario [65] Research Chair in Experimental Therapeutics and Imaging.

References

[1] Siegel R, DeSantis C, Virgo K, Stein K, Mariotto A, Smith T, Cooper D, Gansler T, Lerro C, and Fedewa S, et al (2012). Cancer treatment and survivorship statistics, 2012. *CA Cancer J Clin* **62**, 220–241.

[2] American Cancer Society (2012). Cancer facts and figures 2012; 2012 [Atlanta, GA, USA. Available: http://www.cancer.org/Research/CancerFactsFigures/CancerFactsFigures/cancer-facts-figures-2012].

[3] Ferlay J, Autier P, Boniol M, Heanue M, Colombet M, and Boyle P (2007). Estimates of the cancer incidence and mortality in Europe in 2006. *Ann Oncol* **18**, 581–592.

[4] Stavridis S, Saidi S, Lekovski L, Dohcev S, and Spasovski G (2010). Screening for prostate cancer: a controversy or fact. *Hippokratia* **14**, 170–175.

[5] Djulbegovic M, Beyth RJ, Neuberger MM, Stoffs TL, Vieweg J, Djulbegovic B, and Dahm P (2010). Screening for prostate cancer: systematic review and meta-analysis of randomised controlled trials. *BMJ* **341**, c4543 [9 pp.].

[6] Andriole GL, Crawford ED, Grubb RL, Buys SS, Chia D, Church TR, Fouad MN, Isaacs C, Kvale PA, and Reding DJ, et al (2012). Prostate cancer screening in the randomized Prostate, Lung, Colorectal, and Ovarian Cancer Screening Trial: mortality results after 13 years of follow-up. *J Natl Cancer Inst* **104**, 125–132.

[7] Schröder FH, Hugosson J, Roobol MJ, Tammela TLJ, Ciatto S, Nelen V, Kwiatkowski M, Lujan M, Lilja H, and Zappa M, et al (2009). Screening and prostate-cancer mortality in a randomized European study. *N Engl J Med* **360**, 1320–1328.

[8] Moyer VA (2012). Screening for prostate cancer: U.S. Preventive Services Task Force recommendation statement. *Ann Intern Med* **157**, 120–134.

[9] Wilt TJ and Ahmed HU (2013). Prostate cancer screening and the management of clinically localized disease. *BMJ* **346**, f325 [9 pp.].

[10] Singh PB, Ahmed HU, Simmons L, Freeman A, and Emberton M (2011). Time to rethink PSA screening. *Arch Intern Med* **171**, 595–596.

[11] Kelloff GJ, Choyke P, and Coffey DS (2009). Challenges in clinical prostate cancer: role of imaging. *AJR Am J Roentgenol* **192**, 1455–1470.

[12] Feleppa EJ, Fair WR, Liu T, Kalisz A, Balaji KC, Porter CR, Tsai H, Reuter V, Gnadt W, and Miltner MJ (2000). Three-dimensional ultrasound analyses of the prostate. *Mol Urol* **4**, 133–139 [discussion 141].

[13] Feleppa E, Fair W, Tsai H, Porter C, Balaji K, Liu T, Kalisz A, Lizzi F, Rosado A, and Manolakis D, et al (1999). Progress in two-dimensional and three-dimensional ultrasonic tissue-type imaging of the prostate based on spectrum analysis and nonlinear classifiers. *Mol Urol* **3**, 303–310.

[14] Sadeghi-Naini A, Falou O, Tadayyon H, Al-Mahrouki A, Tran W, Papanicolau N, Kolios MC, and Czarnota GJ (2013). Conventional frequency ultrasonic biomarkers of cancer treatment response in vivo. *Transl Oncol* **6**, 234–243.

[15] Sadeghi-Naini A, Papanicolau N, Falou O, Tadayyon H, Lee J, Zubovits J, Sadeghian A, Karshafian R, Al-Mahrouki A, and Giles A, et al (2013). Low-frequency quantitative ultrasound imaging of cell death in vivo. *Med Phys* **40**, 082901 [13 pp.].

[16] Sadeghi-Naini A, Falou O, Hudson JM, Bailey C, Burns PN, Yaffe MJ, Stanisz GJ, Kolios MC, and Czarnota GJ (2012). Imaging innovations for cancer therapy response monitoring. *Imaging Med* **4**, 311–327.

[17] Sadeghi-Naini A, Falou O, and Czarnota GJ (2012). Quantitative ultrasound visualization of cell death: emerging clinical applications for detection of cancer treatment response. 34th Annual International Conference of the IEEE Engineering in Medicine and Biology Society (EMBC). San Diego, CA, USA: IEEE; 2012. p. 1125–1128.

[18] Sadeghi-Naini A, Falou O, and Czarnota GJ (2012). Quantitative ultrasound spectral parametric maps: early surrogates of cancer treatment response. 34th Annual International Conference of the IEEE Engineering in Medicine and Biology Society (EMBC). San Diego, CA, USA: IEEE; 2012. p. 2672–2675.

[19] Sadeghi-Naini A, Papanicolau N, Falou O, Zubovits J, Dent R, Verma S, Trudeau M, Boileau JF, Spayne J, and Iradji S, et al (2013). Quantitative ultrasound evaluation of tumor cell death response in locally advanced breast cancer patients receiving chemotherapy. *Clin Cancer Res* **19**, 2163–2174.

[20] Sadeghi-Naini A, Sannachi L, Pritchard K, Trudeau M, Gandhi S, Wright FC, Zubovits J, Yaffe MJ, Kolios MC, and Czarnota GJ (2014). Early prediction of therapy responses and outcomes in breast cancer patients using quantitative ultrasound spectral texture. *Oncotarget* **5**, 3497–3511.

[21] Feleppa EJ, Kalisz A, Sokil-Melgar JB, Lizzi FL, Rosado AL, Shao MC, Fair WR, Cookson MS, Reuter VE, and Heston WDW (1996). Typing of prostate tissue by ultrasonic spectrum analysis. *IEEE Trans Ultrason Ferroelectr Freq Control* **43**, 609–619.

[22] Lizzi FL, Astor M, Liu T, Deng C, Coleman DJ, and Silverman RH (1997). Ultrasonic spectrum analysis for tissue assays and therapy evaluation. *Int J Imaging Syst Technol* **8**, 3–10.

[23] Oelze ML and Zachary JF (2006). Examination of cancer in mouse models using high-frequency quantitative ultrasound. *Ultrasound Med Biol* **32**, 1639–1648.

[24] Oelze ML and O'Brien WD (2006). Application of three scattering models to characterization of solid tumors in mice. *Ultrason Imaging* **28**, 83–96.

[25] Lizzi FLL, Astor M, Feleppa EJJ, Shao M, and Kalisz A (1997). Statistical framework for ultrasonic spectral parameter imaging. *Ultrasound Med Biol* **23**, 1371–1382.

[26] Feleppa EJ, Mamou J, Porter CR, and Machi J (2011). Quantitative ultrasound in cancer imaging. *Semin Oncol* **38**, 136–150.

[27] Balaji KC, Fair WR, Feleppa EJ, Porter CR, Tsai H, Liu T, Kalisz A, Urban S, and Gillespie J (2002). Role of advanced 2 and 3-dimensional ultrasound for detecting prostate cancer. *J Urol* **168**, 2422–2425.

[28] Feleppa EJ (2008). Ultrasonic tissue-type imaging of the prostate: implications for biopsy and treatment guidance. *Cancer Biomark* **4**, 201–212.

[29] Mamou J, Coron A, Oelze ML, Saegusa-Beecroft E, Hata M, Lee P, Machi J, Yanagihara E, Laugier P, and Feleppa EJ (2011). Three-dimensional high-frequency backscatter and envelope quantification of cancerous human lymph nodes. *Ultrasound Med Biol* **37**, 345–357.

[30] König A and Klauss V (2007). Virtual histology. *Heart* **93**, 977–982.

[31] Clarke GM, Eidt S, Sun L, Mawdsley G, Zubovits JT, and Yaffe MJ (2007). Whole-specimen histopathology: a method to produce whole-mount breast serial sections for 3-D digital histopathology imaging. *Histopathology* **50**, 232–242.

[32] Yao LX, Zagzebski JA, and Madsen EL (1990). Backscatter coefficient measurements using a reference phantom to extract depth-dependent instrumentation factors. *Ultrason Imaging* **12**, 58–70.

[33] Dong F, Madsen EL, MacDonald MC, and Zagzebski JA (1999). Nonlinearity parameter for tissue-mimicking materials. *Ultrasound Med Biol* **25**, 831–838.

[34] Sahoo PK, Farag AA, and Yeap Y-P (1992). Threshold selection based on histogram modeling. IEEE International Conference on Systems, Man, and Cybernetics. Chicago, IL, USA: IEEE; 1992. p. 351–356.

[35] Joo S, Yang YS, Moon WK, and Kim HC (2004). Computer-aided diagnosis of solid breast nodules: use of an artificial neural network based on multiple sonographic features. *IEEE Trans Med Imaging* **23**, 1292–1300.

[36] Lizzi FL, Ostromogilsky M, Feleppa EJ, Rorke MC, and Yaremko MM (1987). Relationship of ultrasonic spectral parameters to features of tissue microstructure. *IEEE Trans Ultrason Ferroelectr Freq Control* **34**, 319–329.

[37] Feleppa EJ (2008). Cancer of the prostate (PCa). *Cancer Biomark* **4**, 193–194.

[38] Feleppa EJ, Porter CR, Ketterling J, Lee P, Dasgupta S, Urban S, and Kalisz A (2004). Recent developments in tissue-type imaging (TTI) for planning and monitoring treatment of prostate cancer. *Ultrason Imaging* **26**, 163–172.

[39] Feleppa EJ, Ennis RD, Schiff PB, Wuu C-S, Kalisz A, Ketterling J, Urban S, Liu T, Fair WR, and Porter CR, et al (2002). Ultrasonic spectrum-analysis and neural-network classification as a basis for ultrasonic imaging to target brachytherapy of prostate cancer. *Brachytherapy* **1**, 48–53.

[40] Feleppa EJ, Ennis RD, Schiff PB, Wuu CS, Kalisz A, Ketterling J, Urban S, Liu T, Fair WR, and Porter CR, et al (2001). Spectrum-analysis and neural networks for imaging to detect and treat prostate cancer. *Ultrason Imaging* **23**, 135–146.

[41] Vlad RM, Kolios MC, and Czarnota GJ (2011). Ultrasound imaging of apoptosis: spectroscopic detection of DNA-damage effects at high and low frequencies. *Methods Mol Biol* **682**, 165–187.

[42] Banihashemi B, Vlad R, Debeljevic B, Giles A, Kolios MC, and Czarnota GJ (2008). Ultrasound imaging of apoptosis in tumor response: novel preclinical monitoring of photodynamic therapy effects. *Cancer Res* **68**, 8590–8596.

[43] Czarnota GJ, Kolios MC, Vaziri H, Benchimol S, Ottensmeyer FP, Sherar MD, and Hunt JW (1997). Ultrasonic biomicroscopy of viable, dead and apoptotic cells. *Ultrasound Med Biol* **23**, 961–965.

[44] Czarnota GJ, Kolios MC, Abraham J, Portnoy M, Ottensmeyer FP, Hunt JW, and Sherar MD (1999). Ultrasound imaging of apoptosis: high-resolution non-invasive monitoring of programmed cell death in vitro, in situ and in vivo. *Br J Cancer* **81**, 520–527.

[45] Mamou J, Ramachandran S, and Feleppa EJ (2008). Angle-dependent ultrasonic detection and imaging of brachytherapy seeds using singular spectrum analysis. *J Acoust Soc Am* **123**, 2148–2159.
[46] Alam SK, Mamou J, Feleppa EJ, Kalisz A, and Ramachandran S (2011). Comparison of template-matching and singular-spectrum-analysis methods for imaging implanted brachytherapy seeds. *IEEE Trans Ultrason Ferroelectr Freq Control* **58**, 2484–2491.
[47] Mamou J and Feleppa EJ (2007). Singular spectrum analysis applied to ultrasonic detection and imaging of brachytherapy seeds. *J Acoust Soc Am* **121**, 1790–1801.
[48] Deftereos S, Giannopoulos G, Kossyvakis C, and Pyrgakis VN (2010). Virtual histology. *Hell J Cardiol* **51**, 235–244.
[49] Braeckman J, Autier P, Garbar C, Marichal MP, Soviany C, Nir R, Nir D, Michielsen D, Bleiberg H, and Egevad L, et al (2008). Computer-aided ultrasonography (HistoScanning): a novel technology for locating and characterizing prostate cancer. *BJU Int* **101**, 293–298.
[50] Braeckman J, Autier P, Soviany C, Nir R, Nir D, Michielsen D, Treurnicht K, Jarmulowicz M, Bleiberg H, and Govindaraju S, et al (2008). The accuracy of transrectal ultrasonography supplemented with computer-aided ultrasonography for detecting small prostate cancers. *BJU Int* **102**, 1560–1565.
[51] Simmons LAM, Autier P, Zát'ura F, Braeckman J, Peltier A, Romic I, Stenzl A, Treurnicht K, Walker T, and Nir D, et al (2012). Detection, localisation and characterisation of prostate cancer by prostate HistoScanning(™). *BJU Int* **110**, 28–35.
[52] Javed S, Chadwick E, Edwards AA, Beveridge S, Laing R, Bott S, Eden C, and Langley S (2014). Does prostate HistoScanning™ play a role in detecting prostate cancer in routine clinical practice? Results from three independent studies. *BJU Int* **114**, 541–548.
[53] Schiffmann J, Tennstedt P, Fischer J, Tian Z, Beyer B, Boehm K, Sun M, Gandaglia G, Michl U, and Graefen M, et al (2014). Does HistoScanning™ predict positive results in prostate biopsy? A retrospective analysis of 1,188 sextants of the prostate. *World J Urol* **32**, 925–930.
[54] Shah V, Pohida T, Turkbey B, Mani H, Merino M, Pinto PA, Choyke P, and Bernardo M (2009). A method for correlating in vivo prostate magnetic resonance imaging and histopathology using individualized magnetic resonance-based molds. *Rev Sci Instrum* **80**, 104301 [6 pp.].
[55] Mazaheri Y, Bokacheva L, Kroon D-J, Akin O, Hricak H, Chamudot D, Fine S, and Koutcher JA, et al (2010). Semi-automatic deformable registration of prostate MR images to pathological slices. *J Magn Reson Imaging* **32**, 1149–1157.
[56] Trivedi H, Turkbey B, Rastinehad AR, Benjamin CJ, Bernardo M, Pohida T, Shah V, Merino MJ, Wood BJ, and Linehan WM, et al (2012). Use of patient-specific MRI-based prostate mold for validation of multiparametric MRI in localization of prostate cancer. *Urology* **79**, 233–239.
[57] Röthke MC, Afshar-Oromieh A, and Schlemmer H-P (2013). Potential of PET/MRI for diagnosis of prostate cancer. *Radiologe* **53**, 676–681.
[58] Turkbey B, Mena E, Aras O, Garvey B, Grant K, and Choyke PL (2013). Functional and molecular imaging: applications for diagnosis and staging of localised prostate cancer. *Clin Oncol* **25**, 451–460.
[59] Mari Aparici C and Seo Y (2012). Functional imaging for prostate cancer: therapeutic implications. *Semin Nucl Med* **42**, 328–342.
[60] Soares R and Eden CG (2014). Surgical treatment of high risk prostate cancer. *Minerva Urol Nefrol* [Epub ahead of print, in press].
[61] Thomsen FB, Berg KD, Røder MA, Iversen P, and Brasso K (2014). Active surveillance for localized prostate cancer: an analysis of patient contacts and utilization of healthcare resources. *Scand J Urol* . http://dx.doi.org/10.3109/21681805.2014.970572 [Epub ahead of print, in press].
[62] Bhatnagar V, Stewart ST, Bonney WW, and Kaplan RM (2004). Treatment options for localized prostate cancer: quality-adjusted life years and the effects of lead-time. *Urology* **63**, 103–109.
[63] http://banting.fellowships-bourses.gc.ca/home-accueil-eng.html.
[64] http://www.chairs-chaires.gc.ca/home-accueil-eng.aspx.
[65] https://www.cancercare.on.ca/.